

NEAR-EQUIPARTITION JETS WITH LOG-PARABOLA ELECTRON ENERGY DISTRIBUTION AND THE BLAZAR SPECTRAL-INDEX DIAGRAMS

CHARLES D. DERMER,¹ DAHAI YAN,^{2,3} LI ZHANG,³ JUSTIN D. FINKE,¹ & BENOIT LOTT⁴

Draft version July 23, 2015

ABSTRACT

Fermi-LAT analyses show that the γ -ray photon spectral indices Γ_γ of a large sample of blazars correlate with the νF_ν peak synchrotron frequency ν_s according to the relation $\Gamma_\gamma = d - k \log \nu_s$. The same function, with different constants d and k , also describes the relationship between Γ_γ and peak Compton frequency ν_C . This behavior is derived analytically using an equipartition blazar model with a log-parabola description of the electron energy distribution (EED). In the Thomson regime, $k = k_{EC} = 3b/4$ for external Compton processes and $k = k_{SSC} = 9b/16$ for synchrotron self-Compton (SSC) processes, where b is the log-parabola width parameter of the EED. The BL Lac object Mrk 501 is fit with a synchrotron/SSC model given by the log-parabola EED, and is best fit away from equipartition. Corrections are made to the spectral-index diagrams for a low-energy power-law EED and departures from equipartition, as constrained by absolute jet power. Analytic expressions are compared with numerical values derived from self-Compton and external Compton scattered γ -ray spectra from Ly α broad-line region and IR target photons. The Γ_γ vs. ν_s behavior in the model depends strongly on b , with progressively and predictably weaker dependences on γ -ray detection range, variability time, and isotropic γ -ray luminosity. Implications for blazar unification and blazars as ultra-high energy cosmic-ray sources are presented. Arguments by Ghisellini et al. (2014) that the jet power exceeds the accretion luminosity depend on the doubtful assumption that we are viewing at the Doppler angle.

Subject headings: gamma rays: galaxies—radiation mechanisms: nonthermal—galaxies: jets—galaxies: BL Lacertae objects: general—galaxies: quasars: general—acceleration of particles

1. INTRODUCTION

Searches for an ordering principle in blazar science have met with limited success. One of the most debated is the *blazar sequence*, in which blazar data seem to show an inverse correlation between apparent isotropic synchrotron luminosity L_{syn} and peak synchrotron frequency ν_s of the blazar νF_ν spectral energy distribution (SED) (Fossati et al. 1998; Sambruna et al. 1996). This behavior, which is mirrored in the γ -ray regime, has been interpreted in terms of cooling processes (Ghisellini et al. 1998; Böttcher & Dermer 2002; Finke 2013). The validity of the blazar sequence has, however, been criticized (Giommi et al. 2012, 2013) as possibly resulting from spurious correlations introduced by combining samples from radio and X-ray blazar surveys, problems from redshift incompleteness, and confusing lineless BL Lac objects that lack accretion disk with those where the BLR radiation is overwhelmed by beamed emission. Contrary to the simple blazar sequence, Meyer et al. (2011) present evidence for the existence of two separate tracks in the L_{syn} vs. ν_s plane, including radio galaxies in the blazar-sequence plot.

A second strong correlation is the *blazar divide*. From the first three months of Fermi Large Area Telescope

(LAT) blazar data, Ghisellini et al. (2009) argued that hard ($\Gamma_\gamma < 2$) γ -ray spectrum blazars are associated with sources radiating isotropic γ -ray luminosities $L_\gamma \lesssim 5 \times 10^{46}$ erg s^{−1}, while soft ($\Gamma_\gamma > 2$) γ -ray blazars are more likely to be at larger values of L_γ . From the Second Fermi LAT AGN (2LAC) data (Ackermann et al. 2011), a broad divide is evident in the direct data at $L_\gamma \cong 10^{46}$ erg s^{−1} (Figs. 37 and 38 in Ackermann et al. 2011), though with no other apparent dependence of Γ_γ on L_γ in the ranges $10^{44} \lesssim L_\gamma \lesssim 10^{46}$ erg s^{−1} and $10^{46} \lesssim L_\gamma \lesssim 10^{49}$ erg s^{−1}. In terms of a beaming-corrected Eddington ratio ℓ_{Edd} for a black hole with mass $\sim 10^9 M_\odot$, this could imply a transition from an inefficiently radiating ADAF-type flow at $\ell_{Edd} \lesssim 0.01$ to a thick disk when $\ell_{Edd} \gtrsim 0.01$ (Ghisellini et al. 2009). The γ -ray Compton dominance \mathcal{A}_C , which is essentially the ratio of the bolometric γ -ray and synchrotron luminosities, also strongly correlates with ν_s (Fossati et al. 1998; Finke 2013).

Definitive interpretations of blazar sequence and blazar divide data are hampered by redshift incompleteness. BL Lac objects without redshift information may themselves constitute separate populations in the L_{syn} vs. ν_s or Γ_γ vs. L_γ planes, though large efforts have been made to provide complete, or at least redshift-constrained samples of blazar data (Shaw et al. 2013; Ajello et al. 2014). The \mathcal{A}_C vs. ν_s distributions of 2LAC blazars with and without redshift do not significantly differ (Finke 2013).

A third robust correlation in blazar physics relates γ -ray spectral index Γ_γ with peak synchrotron (ν_s) or peak Compton γ -ray (ν_C) frequencies (in this study, we as-

¹ Space Science Division, U.S. Naval Research Laboratory, Washington, DC 20375, USA. e-mail: charles.dermer@nrl.navy.mil

² Key Laboratory of Particle Astrophysics, Institute of High Energy Physics, Chinese Academy of Sciences, Beijing 100049, China

³ Department of Astronomy, Yunnan University, Kunming 650091, Yunnan, China

⁴ Centre d'Études Nucléaires Bordeaux Gradignan, Université de Bordeaux, CNRS/IN2P3, UMR 5797, Gradignan, 33175, France

sume that the blazar SEDs are made by leptonic processes only).⁵ These *spectral-index diagrams* for FSRQ and BL Lac blazars have been reported in the First LAT AGN Catalog (1LAC, Fig. 13 in Abdo et al. 2010a), the Fermi Bright Blazar SED paper (Fig. 29 in Abdo et al. 2010b), the 2LAC (Fig. 17 in Ackermann et al. 2011), and the 3LAC (Fig. 10 in Ackermann et al. 2015). The distributions of spectral indices of the entire BL Lac and FSRQ blazar samples follow a pattern, with large scatter, described by the relation $\Gamma_\gamma = d - k \log \nu_{14}$, where $\nu_s = 10^{14} \nu_{14}$ Hz. For the entire sample of FSRQs and BL Lac objects, the value $k = 0.18 \pm 0.03$ is found in Ackermann et al. (2015). A similar function, with different values of d and k , apply to the Γ_γ vs. ν_C data. The spectral-index distribution of BL Lac objects with unknown redshift is generally consistent with the distribution of BL Lac objects with known redshift (Ackermann et al. 2011, 2015).

In this paper, we use an equipartition blazar modeling approach (Cerruti et al. 2013; Dermer et al. 2014a) by assuming a log-parabola electron energy distribution (EED) to explain the blazar spectral-index diagrams. In Section 2 we derive analytic Thomson-regime expressions for the relationship between Γ_γ and ν_s , depending on whether the γ rays are made through external Compton (EC) or synchrotron self-Compton (SSC) processes. Because of the equipartition relations, the expressions depend on b , ν_s , variability time t_{var} , bolometric isotropic synchrotron luminosity L_{syn} , an equipartition parameter ζ_e and a radiation parameter ζ_s . The simpler Γ_γ vs. ν_C expressions are also obtained. The derived analytic relations, confirmed by numerical modeling, are shown in Section 3 to be in general accord with the blazar spectral-index diagram data, whether external radiation fields in the jet environment are present or absent. The effects of a log-parabola EED with a low-energy power-law component are also considered.

In Section 4, application of the equipartition model to the BL Lac object Mrk 501 is demonstrated, and effects of departures from equipartition are evaluated. Trends in spectral-index behavior with other observables constrained can be tested with correlated Fermi-LAT and multiwavelength data, and how this work relates to the blazar sequence and blazar divide, and blazars as UHECR sources, are discussed in Section 5. The work is summarized in Section 6.

Appendix A gives a Thomson-regime derivation of the SSC spectrum with a log-parabola electron distribution, and Appendix B gives a jet power-analysis. There we show that the assumption that blazars are typically observed at the Doppler beaming angle may have led Ghisellini et al. (2014) to overestimate the absolute jet power. Indeed, out-of-equipartition models are ultimately constrained by demands for power.

2. EQUIPARTITION BLAZAR MODELING WITH LOG-PARABOLA ELECTRON ENERGY DISTRIBUTION

A standard blazar-jet model, treated in innumerable blazar spectral modeling papers (see Böttcher et al. 2012, for review), starts with magnetized plasma that is

ejected at relativistic speeds along the poles of a rotating black hole.⁶ The jet plasma, which entrains thermal and nonthermal particles in a hypothetical tangled and randomly oriented magnetic field, is a source of escaping photons, and potentially also of escaping cosmic rays and neutrinos. The jet power is extracted from the mass energy of accreting matter and/or the rotational energy of the black hole itself. The collimated relativistic plasma outflow, an exhaust byproduct of the energy generated by the black-hole engine, is usually attributed to processes taking place in the magnetosphere of the rotating black hole. The polarized broad-band synchrotron radiation emitted by an energetic EED (which could also contain positrons) is boosted by the Doppler effect along the jet axis, so that rapidly variable jet synchrotron radiation can be detected by Earth-based observatories from large redshift ($z \gg 1$) sources.

The jet electrons also Compton scatter ambient photons to γ -ray energies. Besides the accompanying SSC emission from target synchrotron photons (e.g., Maraschi et al. 1992; Bloom & Marscher 1996), EC γ rays are made when the nonthermal jet electrons scatter photons from external radiation fields. Depending on jet Doppler factor δ_D and BLR cloud parameters, the direct accretion-disk radiation field dominates the external radiation field of a powerful FSRQ at $\ll 10^3$ Schwarzschild radii, BLR fields are strongest within ~ 0.3 pc (Dermer et al. 1992; Sikora et al. 1994; Dermer & Schlickeiser 2002), while at the pc scale and beyond, infrared radiation from a surrounding IR-emitting dust torus would have the largest energy density of all ambient radiation fields (Błażejowski et al. 2000; Sikora et al. 2009; Ghisellini & Tavecchio 2009) in the inner blazar-jet environment.

The form of the nonthermal EED is often treated by either assuming a nonthermal injection spectrum of leptons that evolves in response to adiabatic and radiative losses, or by assuming a form for the average steady-state EED in the radiating jet plasma. Adopting the latter approach, we assume that the 3 parameter log-parabola function

$$\gamma'^2 N'_e(\gamma') = [\gamma'^2_{pk} N'_e(\gamma'_{pk})] \left(\frac{\gamma'}{\gamma'_{pk}} \right)^{-b \log(\frac{\gamma'}{\gamma'_{pk}})} \equiv K' y^{-b \log y} \quad (1)$$

provides an approximate description of the nonthermal lepton spectrum. Here $y \equiv \gamma'/\gamma'_{pk}$, γ'_{pk} is the peak, or principal, Lorentz factor of the fluid-frame EED, eq. (1). The value of K' can be related to either the total particle number or total comoving particle energy (Dermer et al. 2014a); in the latter case, $K' = \mathcal{E}'_e / m_e c^2 \sqrt{\pi \ln 10 / b}$, where \mathcal{E}'_e is the nonthermal electron energy of the blob.

The continuously curving EED given by a log-parabola function derives from stochastic acceleration processes with radiation and escape (see, e.g., Massaro et al. 2004; Becker et al. 2006; Tramacere et al. 2007, 2011; Stawarz & Petrosian 2008). With this form of the EED, GeV breaks in FSRQs and blazars with $\nu_{pk}^{syn} \lesssim 10^{14}$ Hz are shown to arise from the onset of Klein-Nishina effects when scattering BLR photons (Cerruti et al. 2013;

⁵ A correlation of the log-parabola width parameter b and ν_s is apparent in SED modeling studies (Chen 2014), but is based on only 5 or 6 high-synchrotron peaked blazars.

⁶ The shock-in-jet model of Marscher & Gear (1985) provides an alternate approach that could apply to the $\ll 10^{12}$ Hz radio regime that often remains unfit in the standard model described here.

TABLE 1
DEPENDENCES OF δ_D , B' , AND γ'_{pk} ^a

	Coef.	L_{48}	ν_{14}	t_4	ζ_s	ζ_e	f_0	f_1	f_2
δ_D	17.5	3/16	1/8	-1/8	-7/16	1/4	-7/16	-1/4	-1/8
$B'(G)$	5.0	-1/16	-3/8	-5/8	13/16	-3/4	13/16	3/4	3/8
γ'_{pk}	523	-1/16	5/8	3/8	-3/16	1/4	-3/16	-1/4	-5/8
\mathcal{E}^b	1.4	5/16	-1/8	1/8	-1/16	-1/4	-11/16	1/4	1/8
$L_{jet,B}^c$	4	5/8	-1/4	1/4	-1/8	-1/2	-1/8	1/2	1/4

^a So, e.g., $\delta_D \cong 17.5 L_{48}^{3/16} (\nu_{14}/f_2 t_4)^{1/8} (f_0 \zeta_s)^{-7/16} (\zeta_e/f_1)^{1/4}$, etc.

^b $\mathcal{E} = E_{max}(10^{20} \text{ eV})/Z$

^c Absolute power in magnetic field, units of $10^{44} \text{ erg s}^{-1}$

Ackermann et al. 2010; Tavecchio & Ghisellini 2008), and to give (Dermer et al. 2014a) reasonable fits to four epochs of quasi-simultaneous multiwavelength observations of 3C 279 (Hayashida et al. 2012). As we show below, this approach also gives good fits to the SED of Mrk 501, though the best fits are achieved with an electron distribution out of equipartition with the magnetic field.

The comoving synchrotron luminosity

$$L'_{syn} = c\sigma_T \frac{B'^2}{6\pi} \int_1^\infty d\gamma' \gamma'^2 N_e(\gamma') \quad (2)$$

implies, using Eq. (1) and a δ -function approximation for the synchrotron photon with average dimensionless energy $\epsilon_{syn} = (3/2)\delta_D(B'/B_{cr})\gamma'^2$ (Dermer & Menon 2009), the received synchrotron luminosity spectrum

$$\epsilon L_{syn}(\epsilon) = v x^{1-\hat{b} \ln x} = v \left(\frac{\epsilon}{\epsilon_{pk}} \right)^{\frac{1}{2} - \frac{b}{4} \log(\epsilon/\epsilon_{pk})}, \quad (3)$$

where $x = \sqrt{\epsilon/\epsilon_{pk}}$, $v = f_3 L_{syn}$, and $f_3^{-1} = 2 \cdot 10^{1/4b} \sqrt{\pi \ln 10/b}$ (Dermer et al. 2014a). Thus the effective log-parabola width parameter b_{sy} for the synchrotron spectrum is given by $b_{sy} = b/4$ in the δ -function approximation, and $b_{sy} \cong b/5$ when using the full Thomson cross section (Massaro et al. 2006; Paggi et al. 2009). The peak synchrotron frequency $\epsilon_{pk} = (3/2)\delta_D(B'/B_{cr})\gamma'^2_{pk}$. The slope of the $\epsilon L_{syn}(\epsilon)$ spectrum is

$$\alpha_\nu \equiv \frac{d \ln[\epsilon L_{syn}(\epsilon)]}{d \ln \epsilon} = \frac{1}{2} [1 - b \log(\epsilon/\epsilon_{pk})]. \quad (4)$$

(Massaro et al. 2004a). Because the nonthermal electron energy-loss rate from synchrotron processes scales quadratically with electron Lorentz factor γ' , the synchrotron spectrum from a log-parabola distribution of electrons has a νL_ν synchrotron peak energy $\epsilon_s = h\nu_s/m_e c^2$ that is shifted to higher values than ϵ_{pk} . Eq. (4) shows that $\epsilon_s = 10^{1/b} \epsilon_{pk}$ (Massaro et al. 2006).

Table 1 shows the various dependencies of blob properties on the observables L_{48} , ϵ_s (or ν_{14}), t_{var} and b , and on the equipartition factor ζ_e and radiative factor ζ_s . The factor ζ_e is the ratio of nonthermal electron energy density u'_e to magnetic-field energy density $u'_{B'} = B'^2/8\pi$,

and ζ_s is the ratio the jet-frame synchrotron photon energy density and $u'_{B'}$. In the blob scenario, the geometry factor $f_0 = 1/3$. The b -dependent factors are $f_1 = 10^{-1/4b}$, $f_2 = 10^{1/b}$, and $f_3 = (2 \cdot 10^{1/4b} \sqrt{\pi \ln 10/b})^{-1}$ (Dermer et al. 2014a), so $\epsilon_s = f_2 \epsilon_{pk}$.

The similarity of the underlying physics of the synchrotron and Compton processes (Blumenthal & Gould 1970) means that an expression like eq. (4) holds for Compton scattering in the Thomson regime, except now ϵ_{pk} is replaced by a corresponding peak photon energy for EC and SSC processes (e.g., Paggi et al. 2009). In the EC case, $\epsilon_{pk,EC} = (4/3)\delta_D^2 \epsilon_0 \gamma'^2_{pk}$, assuming an isotropic monochromatic external radiation field with energy ϵ_0 and energy density u_0 . From the equipartition relations (Dermer et al. 2014a) shown in Table 1 for the photon spectral index $\Gamma_\gamma = 2 - \alpha_\nu$, we find that the photon index for EC processes is given by

$$\Gamma_\gamma^{EC} \cong \frac{17}{8} + \frac{b}{2} \log \left(\frac{f_0^{5/4} E_{GeV} \zeta_s^{5/4}}{\epsilon_{Ly\alpha} t_4^{1/2} \zeta_e L_{48}^{1/4}} \right) - \frac{3b}{4} \log \nu_{14}. \quad (5)$$

Here E_{GeV} is the effective detection energy in GeV, and $\epsilon_0 = 2 \times 10^{-5} \epsilon_{Ly\alpha}$ for Ly α /BLR scattering. A nominal value of $E_{GeV} = 1$ is chosen because the Fermi-LAT is most sensitive at ≈ 1 GeV (Fig. 18 in Abdo et al. 2010c, for a $\Gamma_\gamma = 2.2$ source spectrum). The dependence of Γ_γ on E_{GeV} can be studied by analyzing Fermi-LAT data in discrete energy ranges.

Scattering the dusty torus emission, with IR photon energies corresponding to $\epsilon_{Ly\alpha} \sim 0.02$, implies a Thomson spectrum softer by $\Delta\Gamma_\gamma \cong 0.85b$, because γ -ray photons at a given observing energy are produced in the softer part of the Compton-scattered spectrum when the target photons have lower energies. If equipartition is instead made to total particle energy density u'_{tot} according to the factor $\zeta_{eq} = u'_{tot}/u'_{B'}$, then $\zeta_e = \zeta_{eq}/(1 + \eta_{bl})$ and $\eta_{bl} = u'_{baryons}/u'_e$ is the baryon loading, and $u'_{baryons}$ is the internal energy density in protons and ions (Dermer et al. 2014b, and Appendix B).

The specific spectral synchrotron luminosity, from eq. (3) in the δ -function approximation and results of Dermer et al. (2014a), is given by

$$\epsilon L_{syn}(\epsilon, \Omega) = f_3 N_e \frac{4}{3} c\sigma_T \frac{B'^2}{8\pi} \gamma'^2_{pk} \delta_D^4 x^{1-b \log x}, \quad (6)$$

where $x = \sqrt{\epsilon/\epsilon_{pk}}$, and $\epsilon_{pk} = 4\delta_D B' \gamma'^2_{pk}/3B_{cr}$. The specific spectral γ -ray luminosity in the Thomson regime for a jet traveling through an external isotropic, monochromatic radiation field with frequency $m_e^2 \epsilon_0/h$ and energy density u_0 , in units of $m_e c^2 \text{ cm}^{-3}$, using a δ -function approximation for Thomson scattering, is

$$\epsilon L_{EC}(\epsilon, \Omega) \cong f_3 N_e \frac{4}{3} c\sigma_T u_0 \gamma'^2_{pk} \delta_D^6 v^{1-b \log v}, \quad (7)$$

where $v \equiv \sqrt{\epsilon/\epsilon_{pk,EC}}$ and $\epsilon_{pk,EC} = (4/3)\delta_D^2 \gamma'^2_{pk} \epsilon_0$. The technique of Georganopoulos et al. (2001) is used to derive this expression. The ratio of the spectral synchrotron and Thomson luminosities at their respective peak frequencies is $\delta_D^2 u_0/u'_{B'}$.

For the SSC process, the combined effects of the widths of both the EED and the target synchrotron photon spectrum will broaden the Compton-scattered photon spectrum such that its effective width in the Thomson

regime is obtained by replacing b by $b_{SSC} = b/2$ in eq. (4) (Paggi et al. 2009) and replacing ϵ_{pk} by $\epsilon_{pk,SSC} = 2\delta_D(B'/B_{cr})\gamma_{pk}^4$, giving

$$\Gamma_\gamma^{SSC} = \frac{65}{32} + \frac{b}{4} \log \left(\frac{6.5 \times 10^3 E_{GeV} f_0^{3/8} \zeta_s^{3/8} L_{48}^{1/8}}{\zeta_e^{1/2} t_4^{3/4}} \right) - \frac{9b}{16} \log \nu_{14}, \quad (8)$$

from Table 1. Note that the νL_ν peak SSC frequency is a factor $10^{2/b}$ larger than $\epsilon_{pk,SSC}$. The SSC expression is justified by a more detailed derivation in Appendix A. The uncertainty $\Delta\Gamma_\gamma$ in the spectral index related to geometrical uncertainties can be estimated by letting f_0 range from unity for a blast-wave shell geometry to $f_0 = 1/3$ for a comoving spherical-blob geometry. From eqs. (5) and (8), one can see that this translates into an uncertainty $\Delta\Gamma_\gamma^{EC} \cong 0.30b$ for EC processes and an uncertainty $\Delta\Gamma_\gamma^{SSC} \cong 0.04b$ for SSC processes.

We also derive the Thomson-regime expressions

$$\Gamma_\gamma^{EC,\gamma} = 2 + \frac{b}{2} \log(2.4 E_{GeV}) - \frac{b}{2} \log \nu_{23} \quad (9)$$

for Γ_γ vs. ν_C in EC processes, and

$$\Gamma_\gamma^{SSC,\gamma} = 2 + \frac{b}{4} \log(2.4 E_{GeV}) - \frac{b}{4} \log \nu_{23} \quad (10)$$

for Γ_γ vs. ν_C in SSC processes. Here $\nu_{23} = \nu_C/10^{23}$ Hz is the peak frequency of the Compton component of the νL_ν SED. Note that eq. (9) is independent of the target photon energy, because the expression assumes that the EED and Doppler factor are adjusted to produce a Compton-scattered γ -ray spectrum that peaks at ν_C .

3. MODELING THE BLAZAR SPECTRAL-INDEX DIAGRAM

Fig. 1 shows measured values of Fermi-LAT spectral index Γ_γ from the 2LAC (Ackermann et al. 2011) derived from a single power-law fit to the complete data set in the 0.1 – 100 GeV range for sources with $TS > 25$.⁷ The red, blue, green, and black data symbols correspond, respectively, to γ -ray sources detected with the Fermi-LAT that have been associated with FSRQs, BL Lac objects with and without redshifts, and blazars with optical data too poor to determine if the source is an FSRQ or BL Lac.

From inspection of the plot, it is clear that a function of the form $\Gamma_\gamma = d - k \log \nu_{14}$ will provide a reasonable description of the data. For the entire FSRQ and BL Lac sample, but excluding other blazar candidates, values of $k = 0.18 \pm 0.03$ and $d = 2.25 \pm 0.04$ are deduced in the 3LAC (Ackermann et al. 2015). Comparing this value with the analytic expressions, eqs. (5) and (8), a larger value of b is implied for SSC processes compared to EC processes, but in both cases consistent with $b \approx 1/3$.

The typical value of b can also be deduced from the average nonthermal blazar synchrotron SED, when fit with an expression of the form of Eq. (3). From X-ray analysis of Beppo-SAX data on Mrk 501, Massaro et al. (2004) finds values of b_{sy} ranging from 0.12 – 0.33, implying

⁷ Energy flux is derived in 5 energy bands in intervals defined by 0.1, 0.3, 1, 3, 10 and 100 GeV.

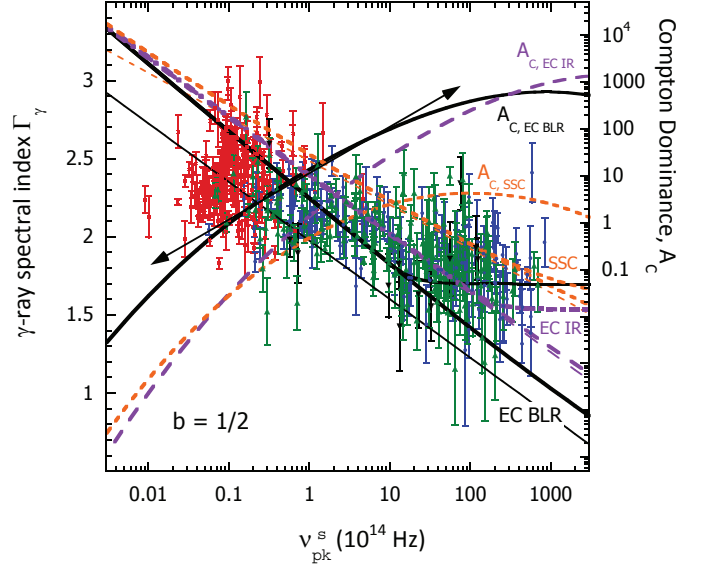


FIG. 1.— Data are the > 100 MeV photon spectral index values Γ_γ as a function of peak synchrotron frequency ν_s for blazars from the 2LAC (Ackermann et al. 2011). Red, blue, green, and black symbols identify, respectively, FSRQs, BL Lac objects with redshifts, BL Lac objects without redshifts, and blazars with data too poor to determine if the source is an FSRQ or a BL Lac object. *Left:* Curves labeled by EC BLR, EC IR and SSC for EC processes with BLR photons, EC processes with IR photons and SSC processes, respectively, show Γ_γ vs. ν_s predictions of the log-parabola equipartition model using standard parameters given by eq. (11). Also, $\epsilon_0 = 2 \times 10^{-5}$ and $u_0 = 10^{-2}$ erg cm $^{-3}$ for Ly α , and $\epsilon_0 = 4.6 \times 10^{-7}$ and $u_0 = 10^{-3}$ erg cm $^{-3}$ for the ~ 1000 K IR radiation. Thick curves give numerical calculations, and thin curves show analytic results, from eqs. (5) and (8). The thick curves that approach constant values at large ν_s are numerical predictions for the power-law, log-parabola model, eq. (12). *Right:* Compton-dominance \mathcal{A}_C as a function of ν_s for EC BLR, EC IR, and SSC processes, as labeled. The line with arrows has a slope of +1 in the \mathcal{A}_C vs. ν_s plane.

a corresponding log-parabola width parameter $b \gtrsim 0.5$. Narrow bandwidth modeling of X-ray synchrotron emission from Mrk 421 gives $b_{sy} \cong 0.3 - 0.5$ (Tramacere et al. 2007), though values of $b_{sy} = 0.17 \pm 0.02$ (2006 15 July pointing), $b_{sy} = 0.11 \pm 0.02$ (2006 April 22 pointing), and $b_{sy} = 0.08 \pm 0.03$ (2006 June 23 pointing) are obtained in more complete joint XRT-BAT analysis (Tramacere et al. 2009), consistent with an electron distribution with $b \cong 5b_{sy} \approx 0.5$. Chen (2014) finds that b_{sy} is distributed in the range $0.05 \lesssim b_{sy} \lesssim 0.25$, implying $0.25 \lesssim b \lesssim 1.25$. More importantly, he finds a dependence of b_{sy} on ν_s , which we discuss further in Section 5. The values of b deduced from spectral modeling tend to be larger than obtained from the slope implied by the spectral-index diagram.

3.1. Standard parameters in log-parabola model

To compare the log-parabola equipartition model with data, we adopt a standard parameter set, and take

$$b = 1/2, \quad t_4 = L_{48} = \zeta_e = \zeta_s = E_{GeV} = 1. \quad (11)$$

The reasoning driving the choice of the standard variability time scale is that the masses of supermassive black holes powering blazars—both FSRQs and BL Lacs—are

typically of the order $\sim 10^9 M_\odot$. The value $t_4 \cong 1$ or $t_{var} \cong 3$ hr corresponds to the light-crossing time across a size equal to the Schwarzschild radius of a $\sim 10^9 M_\odot$ black hole, though of course shorter variability time scales have been recorded during spectacular outbursts of BL Lac objects, including Mrk 421 (Fossati et al. 2008), Mrk 501 (Albert et al. 2007), and PKS 2155-304 (Aharonian et al. 2007), not to mention the extraordinary VHE outburst observed with the MAGIC telescope from the FSRQ PKS 1222+216 with $t_{var} \sim 10$ m (Aleksić et al. 2011). The isotropic synchrotron luminosity L_{syn} can exceed the Eddington limit L_{Edd} , though L_{Edd} is presumably the upper limit to the persistent absolute jet power (see App. B). Standard values $L_{48} \sim 0.1 - 1$ and $L_{48} \sim 10^{-2} - 10^{-3}$ are typical of powerful FSRQs and BL Lac objects, respectively. At the other side of the time domain, $t_{var} \sim 10^5 - 10^6$ s may be compatible with quiet times of blazars.

Fig. 1 shows analytic results of Eqs. (5) and (8) for Γ_γ as a function of $\nu_{pk}^s = \nu_s$, using the standard parameter set. Results of numerical calculations, obtained by modifying the code used in Dermer et al. (2014a), are also shown. The dimensionless photon energies for the BLR and IR photons used in the model are $\epsilon_0 = 2 \times 10^{-5}$ (i.e., 10.2 eV) for BLR photons and $\epsilon_0 = 4.6 \times 10^{-7}$ for warm IR torus dust emission described by an ≈ 1000 K greybody spectrum with $\approx 15\%$ covering factor, giving an energy density of $\approx 10^{-3}$ erg cm $^{-3}$. The analytic results are shown by the thin lines. The numerical results are shown by the thick curves. As can be seen, the analytic SSC and EC IR results are in reasonable agreement with the numerical calculations, whereas the analytic EC BLR results do not agree with the numerical results. Klein-Nishina effects already make themselves felt strongly for target BLR photons scattered to 1 GeV, but only weakly for target IR photons scattered to 1 GeV, as is clear by noting that KN effects set in at photon energies $E_\gamma \gtrsim m_e c^2 / 12 \epsilon_0 \approx 100$ GeV for 1000 K photons, and $E_\gamma \approx 2$ GeV for Ly α photons. The Thomson-regime expressions are harder than the numerical curves because of the Klein-Nishina softening.

Fig. 1 also shows the effects of a low-energy power-law extension of the EED on the spectral-index diagrams. In such a power-law log-parabola (PLLP) model with a low-energy cutoff Lorentz factor γ'_{min} (Yan et al. 2013; Peng et al. 2014), the EED distribution extends eq. (1) by two parameters to take the form

$$\gamma'^2 N'_e(\gamma') = K'_e [y^{2-s} H(y; y_\ell, 1) + y^{2-s-r \log y} H(y-1)]. \quad (12)$$

Here s is the power-law spectral index of the low-energy component, r is a log-parabola width parameter, and $y_\ell = \gamma'_{min}/\gamma_{pk}$. The Heaviside functions are defined such that $H(u) = 1$ when $u \geq 0$ and $H(u) = 0$ otherwise, and $H(u; a, b) = H(u-a)H(b-u)$. The theoretical basis for the form of eq. (12) is discussed below. Results are shown for $s = 2$ and $y_\ell \ll 1$, in which case $r \rightarrow b$, reducing the PLLP model to a 3-parameter model.

3.2. Compton dominance

The numerical results for this particular set of parameters are seen to follow the trend of much of the data. Virtually no FSRQs are observed, however, with $\nu_{14} > 1$. To obtain some insight into this, we calculate the Comp-

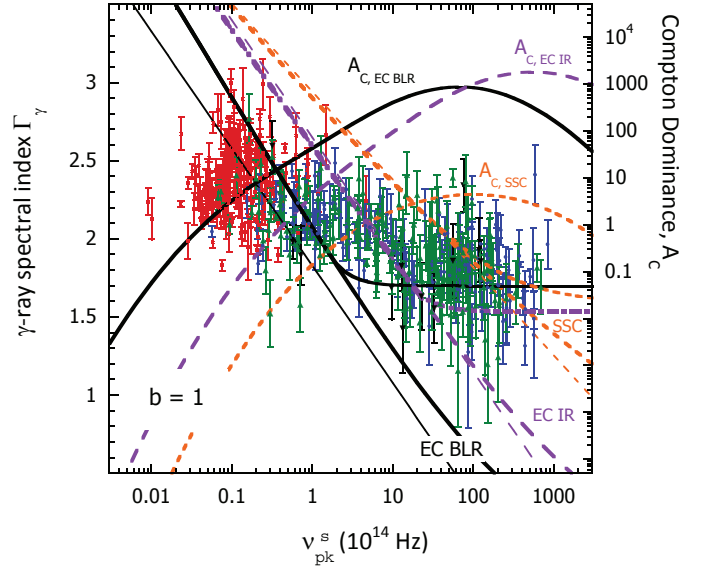


FIG. 2.— Same as Fig. 1, except that $b = 1$. Heavy and light downward-going curves are the numerical and analytic equipartition model predictions, respectively, and upward going curves show Compton dominance for EC BLR, EC IR and SSC processes for the log-parabola EED, eq. (1). The thick curves approaching constant values at large values of ν_s correspond to spectral-index predictions of the PLLP model, eq. (12), with a -2 number index of the low-energy EED.

ton dominance \mathcal{A}_C for our model, defined here as the ratio of the 100 MeV – 100 GeV γ -ray luminosity to the bolometric synchrotron luminosity. It is calculated from the relation

$$\mathcal{A}_C \equiv \frac{L_\gamma(100 \text{ MeV})}{\alpha_\nu L_{syn}} \left[\left(\frac{100}{E_{GeV}} \right)^{\alpha_\nu} - \left(\frac{0.1}{E_{GeV}} \right)^{\alpha_\nu} \right] \quad (13)$$

where α_ν and $L_\gamma(100 \text{ MeV})$ are, respectively, the νL_ν spectral index and luminosity calculated at E_{GeV} GeV. Note that a more detailed and time-intensive calculation would integrate the blazar SED to determine \mathcal{A}_C .

The Compton dominance depends on the energy density of the surrounding radiation fields. For definiteness, we have taken $u_{BLR} = 10^{-2}$ erg cm $^{-3}$ and $u_{IR} = 10^{-3}$ erg cm $^{-3}$ in our calculations. Note that \mathcal{A}_C scales approximately linearly with u_0 . As \mathcal{A}_C becomes progressively smaller, the corresponding blazars becomes progressively less detectable as γ -ray sources. So solutions should be restricted to a minimum value of \mathcal{A}_C . Solutions should also be restricted at large values of \mathcal{A}_C , because Compton drag on the jet becomes a strongly limiting factor, as discussed more in Section 5. Regions where $0.1 \lesssim \mathcal{A}_C \lesssim 30$ may favor LSP blazars to be FSRQs, ISP blazars to the EC BLR, EC IR, and SSC solutions in Fig. 1, as these values bracket measured values of the Compton dominance (Fig. 7 in Finke 2013).

In Fig. 1, we calculate three models in the Γ_γ vs. ν_s plane corresponding to complete dominance either of Ly α BLR radiation (EC BLR), IR radiation from the dusty torus (EC IR), or internal synchrotron radiation (SSC) as the target photon source. Restricting the Compton dominance to $0.1 \lesssim \mathcal{A}_C \lesssim 30$ suggests that most blazars with $\nu_{14} < 0.1$ have γ rays that result from scattered BLR radiation, while blazars with $0.1 \lesssim \nu_{14} \lesssim 1$ would have a mix of blazars with γ rays made by Compton scattering of either BLR or IR photons, or both. At higher peak

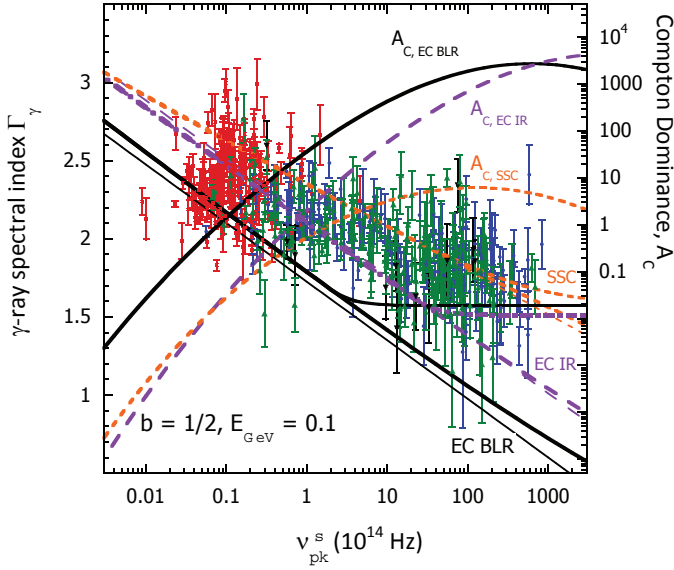


FIG. 3.— Same as Figs. 1 and 2, except that $E_{\text{GeV}} = 0.1$.

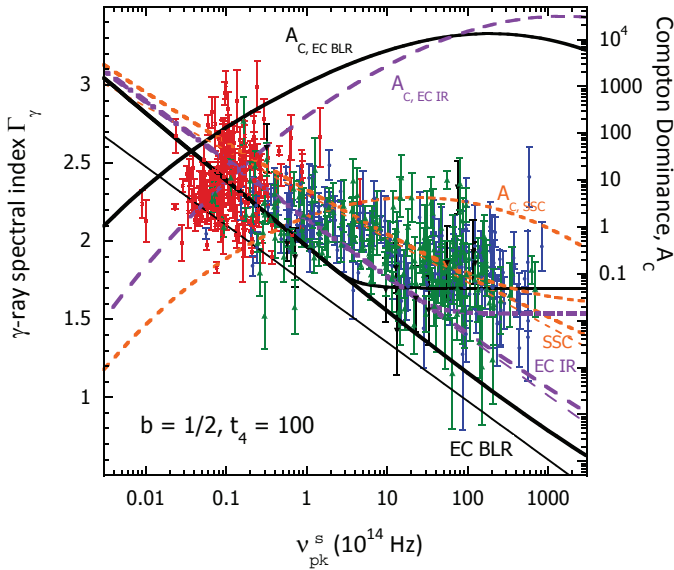


FIG. 4.— Same as Figs. 1 and 2, except that $t_4 = 100$.

synchrotron frequencies, SSC-dominated sources would be most plentiful.

The use of a different model, the PLLP EED, eq. (12) with $s = 2$ and $y_\ell \ll 1$, is displayed in Fig. 1 and subsequent figures by the numerically calculated spectral index curves that approach constant values of spectral index at $\nu_{14} \gg 1$. Klein-Nishina effects, described more below, soften the spectral index below the Thomson regime value of $\Gamma_\gamma = 1.5$. It is interesting that essentially all data are softer than $\Gamma_\gamma = 1.5$, and that smaller values of external radiation energy density could yield typical measured Compton dominance values for ISP and HSP blazars with an external Compton γ -ray component making a significant contribution to the SED.

Figs. 2 – 4 show how changes in the model parameters affect results. Fig. 2 shows that a value of $b = 1$

is incompatible with the combined trend of the data, though a values of $b \cong 1$ may be consistent with subpopulations, e.g., FSRQs. Returning to $b = 1/2$, Fig. 3 shows the effects of calculating the spectral index at $E_{\text{GeV}} = 0.1$, that is, at 100 MeV rather than 1 GeV. Because the Compton-scattered γ -ray SED becomes progressively softer at larger γ -ray energies, the model results in Fig. 3 are uniformly harder than in Fig. 1. The discrepancy between the analytic and numerical results decreases when scattering Ly α radiation because the Klein-Nishina effects on the Compton cross section are not so great when scattering to 100 MeV as compared to 1 GeV. The dependence on detector energy E_{GeV} should clearly show up in Fermi-LAT spectral index diagrams calculated in discrete energy ranges, e.g., 0.3 – 3 GeV and 3 – 30 GeV, and should, in a statistical study, discriminate between EC and SSC processes, though correlations between b and ν_s can hide the effect.

Fig. 4 shows how a slower variability time, with $t_4 = 100$, affects the equipartition spectral-index diagram. Compared to the results in Fig. 1, the effect of longer variability times is to harden the spectrum. From eqs. (5) and (8), the hardening for a factor of 10 longer variability time is $\Delta\Gamma_\gamma^{EC} = -b/4$ for EC processes and $\Delta\Gamma_\gamma^{SSC} = -3b/16$ for SSC processes. Because of the difficulty in measuring t_{var} , the variability effect on spectral index may be too subtle to discriminate between EC and SSC processes. In a statistical sample, however, more rapidly variable sources at equipartition would in general be softer, assuming that there are no underlying correlations between b and t_{var} , and that equipartition holds in the various states.

3.3. Spectral index vs. peak Compton frequency

Fig. 5 shows data from multiwavelength spectral analysis (Abdo et al. 2010b) of 48 bright blazars in the Fermi-LAT Bright AGN Sample (LBAS; Abdo et al. 2009), separated into FSRQs, and low, intermediate, and high synchrotron-peaked (LSP, ISP, and HSP, respectively, defined by whether $\nu_s < 10^{14}$ Hz, $10^{14} < \nu_s$ (Hz) $< 10^{15}$ Hz, or $\nu_s > 10^{15}$ Hz) BL Lac objects. The upper and lower panels gives predictions for the dependence of Γ_γ on ν_C for the equipartition EC and SSC models. The Thomson-regime predictions, eqs. (9) for EC processes and eq. (10) for SSC processes, are plotted in black, depending on whether the γ -ray spectral index is measured at 0.3 GeV (solid curves) or 3 GeV (dashed curves). The index is softer when the γ -ray energy range used to determine the spectral index is larger, as noted above.

It is worth taking a moment to explain the deviations of the numerical curves from the Thomson-regime expressions. Suppose the detector waveband $E_{\text{GeV}} \gg h\nu_C$, corresponding to the left portions of the figures for $E_{\text{GeV}} = 0.3 - 3$. Consider two γ -ray SEDs aligned at the same value of ν_C , one with strong Klein-Nishina effects and one in the Thomson regime. The SED with strong KN effects will be much softer at frequencies $\nu \gg \nu_C$ by comparison with the one in the Thomson regime, causing the softer spectra when $h\nu_C \ll E_{\text{GeV}}$, sometimes dramatically so, compared to SEDs formed by scattering in the Thomson regime.

At the other extreme $h\nu_C \gg E_{\text{GeV}}$, corresponding to the right portions of the figures, the effects of strong

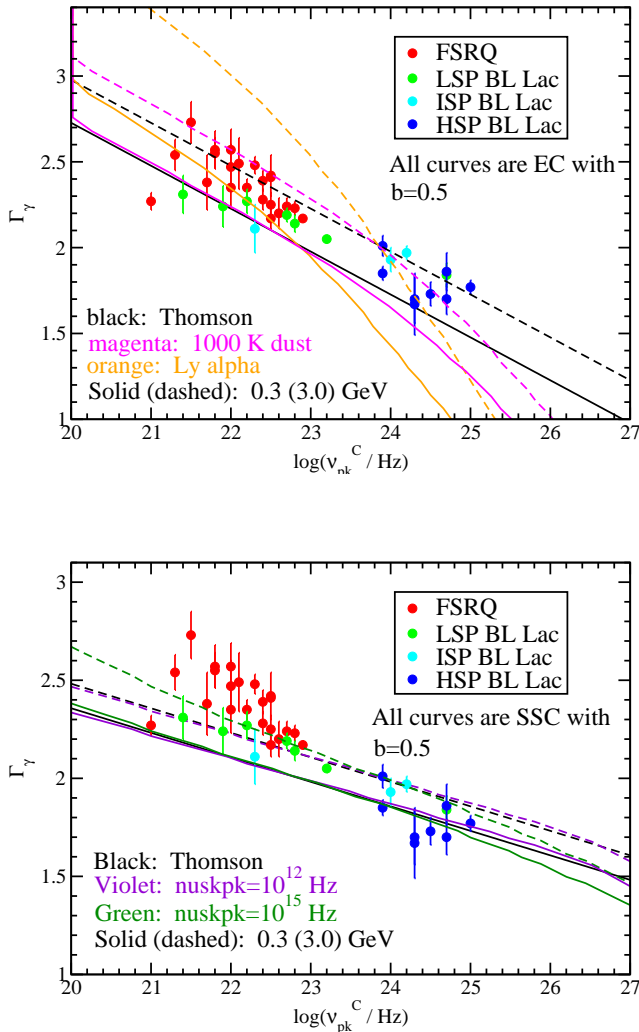


FIG. 5.— Data points show the Fermi-LAT γ -ray spectral index evaluated in the range 0.1–100 GeV as a function of νF_ν peak Compton frequency $\nu_C = \nu_{pk}^C$ of the blazar γ -ray SED (Abdo et al. 2010b). In both panels, the range to calculate the Fermi-LAT spectral index is at 0.3 GeV and 3 GeV for the solid and dashed curves, respectively. (a), upper: Equipartition Thomson-model EC predictions (black) are shown along with numerical predictions evaluated for external 1000 K radiation fields from a dusty torus (magenta curves) and from Ly α radiation (orange), using parameters of Fig. 1 but with $b = 1/2$. (b), lower: Equipartition Thomson-model SSC predictions (black) are shown along with numerical SSC predictions resulting from synchrotron emission with $\nu_s = 10^{12}$ Hz and 10^{15} Hz, as labeled.

KN losses is to harden the low-energy portion of the γ -ray SED compared to an SED formed by scattering in the Thomson regime (and with the same peak Compton frequency). Consequently, Klein-Nishina effects will produce harder spectra when the detector energy range is less than the peak Compton frequency compared to Thomson scattering.

Fig. 5 shows that an EC origin in either BLR or IR radiation is consistent with LSP FSRQ data, but is inconsistent with an SSC origin. A similar conclusion was reached earlier by examining the correlation of Compton dominance with core dominance in FSRQs and BL Lac objects (Meyer et al. 2012). At values of $\nu_C \gg 10^{23}$ Hz, or $E_C \gg 1$ GeV, the sources are all ISP and HSP BL Lac objects, and are compatible with either an SSC or

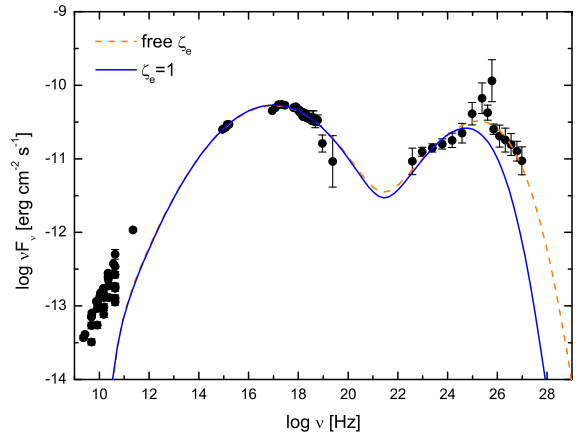


FIG. 6.— Best-fit models for Mrk 501 for fixed $\zeta_e = 1$ and letting ζ_e vary. Data from Abdo et al. (2011), with galactic feature removed.

EC origin of the emission, given the uncertainties in t_{var} . In principle, however, an EC origin can be distinguished from an SSC origin by comparing the curvature of the γ -ray component with that of the synchrotron component.

4. NON-EQUIPARTITION MODEL FOR BL LAC OBJECTS

Blazars may be out of equipartition, though extremely out-of-equipartition blazars would be less favored because of the additional power required. Up to now, we have assumed that the equipartition parameter $\zeta_e = 1$, which minimizes jet power for a given synchrotron SED and variability time, assuming small baryon-loading. Modeling of 3C 279 with $\zeta_e = 1$ was possible in Dermer et al. (2014a), though the very highest energy γ rays were only successfully fit by using long variability times with $t_{var} \approx 10^5 - 10^6$ s, in which case the X-ray emission was not well fit (cf. Hayashida et al. 2012). Better fits were found in the modeling of 3C 454.3 by taking ζ_e between 0.6 and 3.5 (Cerruti et al. 2013), which has a minor effect on the spectral slope relation.⁸

It is worth asking if an equipartition situation applies to BL Lac objects, which would be simpler than FSRQs by lacking significant external radiation fields. We apply the near-equipartition log-parabola (NELP) modeling technique to the 15 March 2009 – 1 Aug 2009 multiwavelength data of the HSP BL Lac object Mrk 501 (Abdo et al. 2011). The data in Fig. 6 include OVRO radio observations, optical data, Swift UVOT and XRT data, GeV γ -ray data from Fermi-LAT, and VHE data from MAGIC. Parameter values are derived using the Markov Chain Monte Carlo (MCMC) technique of Yan et al. (2013) for Mrk 421 and Peng et al. (2014) for Mrk 501, and using the 3-parameter log-parabola electron spectrum, eq. (1). The fit to the TeV data is always bad in the $\zeta_e = 1$ case. The fit with ζ_e allowed to vary is obviously far better.

The distribution of parameter values derived from the MCMC technique for the data of Mrk 501 is shown in

⁸ The fitting published in Cerruti et al. (2013) lacked log-parabola b -dependent factors derived in reply to the referee of Dermer et al. (2014a). Updated values have $\zeta_e \sim 1$ and $\zeta_s \gtrsim 0.2$.

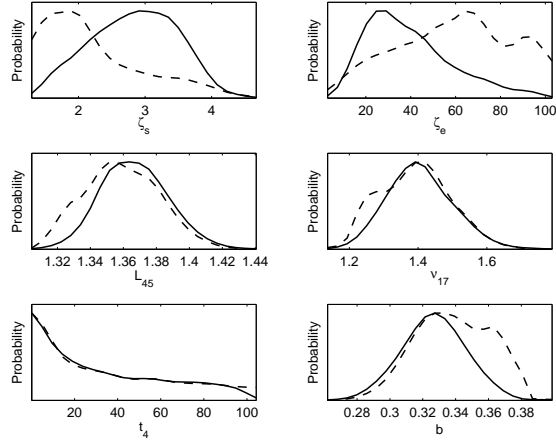


FIG. 7.— Distribution of parameter values for the varying ζ_e case. The dashed curves represent the mean likelihoods of samples and the solid curves are the marginalized probabilities.

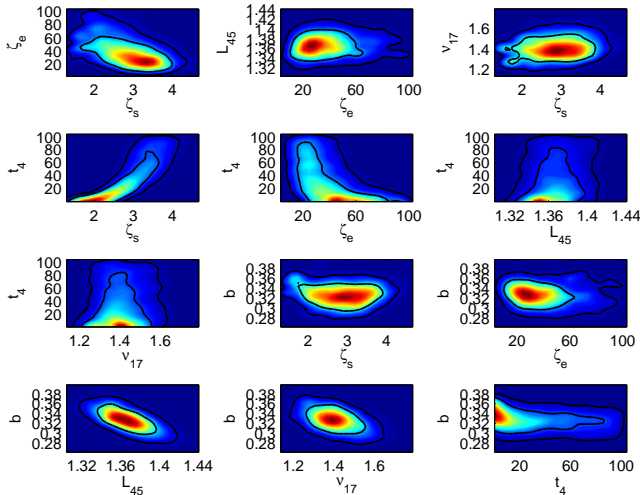


FIG. 8.— Two-dimensional probability contours of parameters.

Fig. 7. The dashed curves are the mean likelihoods of samples and the solid curves are the marginalized probabilities.⁹ In the fits, we run single chains and assume flat priors in the model parameter spaces. Since the MCMC code we used in this paper (Liu et al. 2012; Yuan et al. 2011) is adapted from COSMOMC, we refer the reader to Lewis & Bridle (2002) for a detailed explanation of the code about sampling options, convergence criteria, and statistical quantities. According to the results of Yan et al. (2013), Peng et al. (2014), and Zhou et al. (2014), the MCMC method is well suited to systematically investigate the high-dimensional model parameter spaces in fits to blazar SEDs.

Pairs of values of $\zeta_s \cong 2$, $\zeta_e \cong 70$, and $\zeta_s \cong 3$, $\zeta_e \cong 30$, from the fitting results shown in Fig. 8 correspond to a change in index compared to an equipartition circum-

stance of $\Delta\Gamma_\gamma \cong -0.2b$ and $\Delta\Gamma_\gamma \cong -0.14b$, respectively. Even the large deviation from equipartition causes a spectral-index change $\lesssim 0.1$ unit for $b \cong 0.5$, and even less for $b \cong 1/3$. The typical fluid-frame magnetic field derived from the fits has $B' \approx 10$ mG. Synchrotron self-absorption is included in the fit. Considerations about allowed jet power (see App. B) restrict the departure from equipartition further. Thus deviations from equipartition do not, on the basis of the Mrk 501 case, affect the spectral-index relation significantly.

The inability of the numerical MCMC model to find a most favored value for t_{var} may reflect limitations of the log-parabola EED used to model the Mrk 501 spectrum. Using a model joining a power-law at low electron energies with a log-parabola function at high electron energies, Peng et al. (2014) fit radio data down to \approx GHz frequencies, and obtain preferred variability times of $t_{var} \approx 5 \times 10^5$ s.

For given values of L_{48} and ν_{14} , production of the highest energy γ -ray photons is assisted by going to an electron-dominated regime, where $\zeta_e \gg 1$ and $u'_e \gg u'_{B'}$. The larger Lorentz factor electrons required to produce the same value of ν_s in a weaker magnetic field can Compton scatter ambient photons to the highest energies.

5. DISCUSSION AND SUMMARY

The nonthermal synchrotron paradigm pervades thinking in blazar physics, yet is incapable of explaining some of the most elementary facts, e.g., why synchrotron-radiating nonthermal electrons are apparently accelerated so inefficiently. Rather than reaching values of $\approx 100\Gamma$ MeV (e.g., Guilbert et al. 1983; de Jager et al. 1996), the peak synchrotron frequencies of FSRQs with $\nu_s \cong 10^{13}$ Hz are $\approx 10^{10}$ times less than the highest energy synchrotron photon in the maximally efficient electron Fermi-acceleration scenario. Even the highest energy synchrotron photons from HSP BL Lac objects rarely exceed $\approx 10 - 100$ keV, orders of magnitude below the radiation-reaction limit. It is crucial to understand the reason for the low peak synchrotron frequencies (smaller, of course, than the maximum synchrotron frequency), and how they relate to source luminosities and SEDs, which are the basis of the blazar sequence and blazar divide.

5.1. Near-equipartition, log-parabola (NELP) model

The astrophysics developed here may point a way to the solutions of these puzzles by first explaining the spectral-index diagrams. If the radiating electrons are near equipartition and approximately described by a log-parabola EED because of the underlying acceleration and radiation physics, then the relationships between the γ -ray spectral index Γ_γ and ν_s and ν_C are precisely defined in the Thomson regime by functions of the form $\Gamma_\gamma = d - k \log \nu_{s(C)}$, namely eqs. (5) – (10). The slope is accurately reproduced even when Klein-Nishina effects are important. Moreover, the model inputs are all in principle observable from near-simultaneous multi-wavelength blazar campaigns: L_{48} , ν_s , ν_C and \mathcal{A}_C from spectral observations, b and ζ_s from SED modeling, and t_{var} from temporal analysis. As shown here for Mrk 501, ζ_e and ζ_s can also be deduced from SED modeling, leaving only the baryon-loading η_{bl} as a major uncertainty, which affects the jet power (Appendix B).

⁹ See <http://cosmologist.info/cosmomc/readme.html>

The near-equipartition approach using a 3-parameter log-parabola EED furthermore makes quantitative predictions about the dependence of observables on Γ_γ for statistical quantities of blazars, or for different states of a single blazar. A specific example that can be performed with Fermi-LAT data is to determine γ -ray spectral indices of a large sample of blazars of specific types, e.g., LSP FSRQs and HSP BL Lac objects, in adjacent energy bands, giving the spectral curvature. The curvature of the γ -ray SED is uniquely related to the curvature of the synchrotron SED, depending on whether the γ rays have an SSC or EC origin. The difficulty of performing this test, of course, is the requirement of quasi-simultaneous observations over a large energy range in order to provide a good characterization of the synchrotron SED peak and curvature.

For the synchrotron spectral-index diagram, our analysis shows that $k = k_{EC} = 3b/4$ for EC scattering in the Thomson regime, and $k = k_{SSC} = 9b/16$ for synchrotron self-Compton (SSC) radiation. Numerical results show that this dependence is even valid when Klein-Nishina effects are important. Analysis of the combined sample of FSRQs and BL Lac objects in the 3LAC (Ackermann et al. 2015), $k_{3LAC} = 0.18 \pm 0.03$, implying curvatures of $b \cong 0.24$ if the emission arises from EC processes, and $b \cong 0.32$ if the γ rays are SSC. However, it may not be correct to combine the two samples with different typical values of b in their populations. Specific predictions for the slope of the Γ_γ vs. ν_s behavior, depending on whether the emission has an EC and SSC origin, should be studied for samples of blazars binned in ranges of b , because the two variables are correlated, with larger curvatures, $b \approx 1$ for FSRQs, compared to $b \lesssim 0.5$ for BL Lac objects (Chen 2014). Insofar as the SSC component seems less dominant in FSRQs ($\zeta_s \approx 0.2$) than in BL Lac objects ($\zeta_s \approx 1$), the effect of this correlation on the spectral-index diagrams also has to be considered.

In principle, underlying correlations of Γ_γ with t_{var} can be examined with the increasing number of simultaneous multiwavelength blazar SEDs. Limitations of the log-parabola function to describe the EED remains a central assumption that can be relaxed, though not without associated theoretical or numerical efforts.

5.2. Departures from equipartition

One of the uncertain parameters is the electron equipartition parameter ζ_e , here defined as the ratio of nonthermal electron and positron energy to magnetic-field energy throughout the volume of the radiating region. Assuming $\zeta_e \cong 1$, $\zeta_s = 1$ gives the model predictions shown in the Figs. 1 – 4. As shown in App. B, large departures from equipartition are not allowed if the absolute jet power is required to be less than the accretion power, which in turn is assumed to be bounded by the Eddington luminosity.¹⁰ From the results of App. B, one possibility is that the SSC bolometric luminosity in the SEDs of large Compton-dominance FSRQ flaring events should be small compared to the bolometric synchrotron luminosity (that is, $\zeta_s \ll 1$) for compatibility with sub-Eddington jet powers.

Spectral modeling of the FSRQs 3C 279 and 3C 454.3

¹⁰ Counter-examples to this assumption are claimed (Ghisellini et al. 2014). See App. B.

is possible for $\zeta_e \cong 1$ (Cerruti et al. 2013; Dermer et al. 2014a). For the BL Lac Mrk 501, a large departure from equipartition is required to get a good spectral fit, as we have shown, but even in this case, the effect from this out-of-equipartition condition on Γ_γ is small. The deviations from equipartition giving the best fits to the SEDs of Mrk 501 show that large ζ_e , electron-particle-dominated fits (with correspondingly weak magnetic fields) are favored to fit HSP BL Lacs extending into the TeV regime.

5.3. Extensions of the log-parabola model

The log-parabola function, eq. (1), is motivated by second-order Fermi acceleration theory where MHD turbulence in the emitting fluid systematically accelerates particles to form a curving EED (see Section 2). An equally compelling scenario combining first- and second-order processes considers a power-law distribution of particles injected downstream of a shock into a turbulent region where second-order processes broaden the distribution, so that the EED approximates the PLLP function, eq. (12).

The full PLLP model has 5 parameters, but we have treated in Figs. 1 – 4 the important case of an EED with a -2 number index extending to low energies without cutoff. This EED makes a low-energy boundary to the spectral-index data near the Thomson value of $\Gamma_\gamma = 3/2$. Remarkably, this is as hard as the hardest Fermi-LAT blazar spectral indices measured. So if Compton scattering is responsible for the formation of the γ -ray SEDs of HSP blazars, as is undoubtedly true for the bulk of the radiation, then the PLLP model would give a simple explanation for the lack of blazars harder than $\Gamma_\gamma = 3/2$.

The situation is complicated, however, by the possibility that if the EEDs had low-energy cutoffs rather than power-law extensions to low energies, then HSP blazars in the LAT band would tend to be dim and hard to detect. So the apparent lack of blazars harder than $\Gamma_\gamma = 3/2$ could be a selection effect rather than a limit imposed by the radiation physics. Searches in the Fermi-LAT γ -ray data for blazars harder than $\Gamma_\gamma = 3/2$ would test whether a PLLP model is preferred over a LP model; the detection of such hard blazars would rule out the form of the PLLP considered here.

Except when $\nu_s \gg 10^{16}$ Hz, the existence of a low-energy power law in the EED makes only a small difference to the SSC predictions compared to the pure LP model. Figs. 1 – 4 show that the SSC predictions tend to be slightly softer than the data. A low-energy cutoff in the EED could harden the SEDs, making it possible to attribute an SSC origin to the γ -ray components to all HSP blazars. The discovery of blazars harder than $\Gamma_\gamma = 3/2$ in the Fermi-LAT energy range would support this interpretation.

5.4. Blazar types in the Γ_γ vs. ν_s, ν_C plane

We now ask why there are essentially no FSRQ blazars with $\nu_s \gtrsim 10^{14}$ Hz. The answer is likely to involve the dynamics of increasingly higher synchrotron-peaked near-equipartition jets which, when finding themselves in an external radiation field, are subject to a radiation force opposite to the direction of motion that acts on the nonthermal electron population. In the ideal one-zone model considered here, there is no radiative drag from synchrotron and SSC processes, only from

EC processes (Tramacere et al. 2011). The larger values of δ_D and γ'_{pk} for increasing ν_s implies a correspondingly larger radiative drag when external radiation fields are present that would either slow the jet plasma down (Ghisellini & Tavecchio 2010) or prevent it from reaching such large Γ factors in the first place.

Rather than treating the jet dynamics, which is beyond the scope of the present enquiry, we quote simple analytic expressions for the synchrotron and external Compton SEDs from log-parabola distribution, eqs. (6) and (7), which effectively answers the question of how the Compton dominance (\propto radiative drag) grows with increasing ν_s . From eq. (6), to keep the apparent synchrotron luminosity constant requires $\delta_D^4 B'^2 \gamma_{pk}^2 \sim \text{constant}$. Eq. (7) shows that the apparent external Compton component grows $\propto \delta_D^6 u_0 \gamma_{pk}^2$. The ratio of the EC to synchrotron component is essentially the Compton dominance, which goes $\sim \delta_D^2 u_0 / B'^2 \propto \nu_{14} L_{48}^{1/2} u_0$. So the Compton dominance and radiation drag grow $\propto \nu_{14}$, all other things being equal. This confirms the behavior shown in Figs. 1 – 4, which deviates at large values of ν_{14} due to Klein-Nishina effects. Depending on baryon loading, the jet could be quenched before escaping the BLR, making an unusual, short flaring event. In such an unstable situation, persistent emissions with large ν_{14} in dense external radiation environments might not be possible.

5.5. Maximum particle energy

The near-equipartition log parabola model can be used to derive expressions for maximum escaping proton or ion energy E_{max} . Starting with the Hillas (1984) condition in the form $E_{max} = Z e c B' \delta_D^2 t_{var}$ implies

$$E_{max}(\text{eV}) = 1.4 \times 10^{20} Z L_{48}^{5/16} \left(\frac{t_4}{\nu_{14}} \right)^{1/8} \frac{f_1^{1/4} f_2^{1/8}}{\zeta_e^{1/4} \zeta_s^{1/16} f_0^{11/16}}, \quad (14)$$

using the dependences given in Table 1 for the NELP model. For a BL Lac object with $L_{48} \lesssim 0.01$, the only way to accelerate ultra-high energy cosmic-ray protons to $\gtrsim 10^{20}$ eV occurs when $\zeta_e \ll 1$, that is, in a magnetically-dominated jet. It is interesting to compare this expression with the formula

$$E_{max}(\text{eV}) = 2 \times 10^{20} Z \frac{\sqrt{\epsilon_B (L_{ph}/10^{48} \text{ erg s}^{-1})/\epsilon_e}}{\Gamma/10} \quad (15)$$

(Waxman 2004; Farrar & Gruzinov 2009; Dermer & Razzaque 2010), which was also derived from the Hillas condition, where L_{ph} is the isotropic bolometric photon luminosity, and ϵ_B and ϵ_e are the fractions of jet power going into magnetic field and electrons, respectively.

An interesting feature of a combined lepto-hadronic blazar model using log-parabola functions for the particle distributions is that the synchrotron radiation-reaction limit for protons is $\approx 200\Gamma$ GeV, a factor m_p/m_e greater than the electron limit. The evolution of the combined lepton synchrotron/SSC and proton synchrotron SEDs with ζ_e would favor a proton synchrotron component in the same large magnetization ($\zeta_e \ll 1$) regime where the electrons are incapable of making high-energy radiation.

5.6. Blazar sequence and blazar divide

Multiwavelength data from any given blazar display a rich array of spectral and variability properties. The spectral properties of blazars in this analysis are reduced to ν_s , L_{syn} , ν_C , Γ_γ and b , while the variability properties are reduced to t_{var} .

The spectral-index diagrams show robust correlations, which we explain as a consequence of relativistic blazar jets with different powers and in different environments, within which are entrained relativistic electrons that can be described by log-parabola EEDs. By relating the synchrotron peak frequency and synchrotron SED, which mirrors the EED, to the spectral index of the γ -ray SED formed through EC or SSC processes, the dependence of $\Gamma_\gamma = d - k \log \nu_s$ is easily derived in the Thomson regime. Moreover, the equipartition relations imply specific predictions for underlying correlations.

The spectral-index diagrams are one side of a triangle relating Γ_γ , ν_s (or ν_C), and L^{iso} . The term L^{iso} can either be the apparent isotropic synchrotron, γ -ray, or total bolometric luminosity. The other two sides of the triangle are L^{iso} vs. ν_s or ν_C , the blazar-sequence relations, and Γ_γ vs. L_γ , the blazar-divide relation.

Our work illuminates one side of the triangle, namely Γ_γ vs. ν_s or ν_C . Regarding the blazar divide, suppose as a first approximation that the typical mass of a supermassive black hole is $10^9 M_\odot$, then Fermi-LAT data shows a significant change of spectral index at the Fermi divide of $L_\gamma \cong 10^{46}$ erg s $^{-1}$. If the apparent γ -ray luminosity is 10% of the apparent jet power, and the beaming correction is ~ 100 , then the divide is at $L/L_{Edd} \cong 0.01$ (Ghisellini et al. 2009), and this would also represent the Eddington ratio below which the external radiation field energy density becomes small.

Extremely weak dependences, if any, are seen in the Γ_γ vs. L_γ blazar-divide plots on either side of the divide. Within blazar subpopulations (see Fig. 39 in Ackermann et al. 2011), the dependences of Γ_γ on L_γ are also weak. Other than near the divide itself, there is no clear dependence of Γ_γ on blazar luminosity. Indeed, any such dependence is predicted to be weak, as can be seen from eqs. (5) and (8), which show that $\Gamma_\gamma \propto -b \log L_{syn}/8$ for EC processes, and $\Gamma_\gamma \propto b \log L_{syn}/32$ for SSC processes.

To explain the blazar sequence relating L^{iso} and ν_s or ν_C requires jet physics outside the scope of the present investigation. Rather than saying why blazars of a certain type can exist, however, we can suggest why blazars dominated by EC emission require low-synchrotron peaks. The presence of any appreciable external radiation field would produce a Compton drag that decelerates the bulk flow or prevents such a near-equipartition situation that would produce a synchrotron SED peaking at such large ν_s from forming.

6. SUMMARY

To conclude, we have used an equipartition blazar modeling approach (Cerruti et al. 2013; Dermer et al. 2014a) to explain the correlations of Fermi-LAT γ -ray number spectral index Γ_γ with peak synchrotron frequency ν_s and peak Compton frequency ν_C . This approach assumes a one-zone model fit to the broad-band emission, so that emissions from, e.g., extended VHE jets (Böttcher et al. 2008; Yan et al. 2012), spine-sheath structures (Ghisellini et al. 2005), decelerat-

ing jets (Georganopoulos & Kazanas 2003), or VHE emissions induced by UHECRs produced by the jet (Essey et al. 2010; Takami et al. 2013), are assumed not to affect the γ -ray spectral indices or peak frequencies. Within this framework, the trends in the spectral-index diagrams are reproduced in a model with equipartition conditions and a log-parabola electron distribution with $b \cong 1/2$. This conclusion holds even for out-of-equipartition conditions limited by absolute jet power to be sub-Eddington.

The broadly distributed data in the spectral-index diagrams suggest that a better model comparison would consider a distribution of parameter values to define a preferred model region in the Γ_γ vs. ν_s and ν_C diagrams. Such an approach depends on knowing whether the correlation of b with ν_s (Chen 2014) is robust, if one is to sample from a distribution in b values. Nevertheless, allowed regions in the spectral-index diagrams in Figs. 1 – 5 are already defined by the heavy solid curves, depending on whether internal SSC or external EC BLR or EC IR processes dominate the formation of the γ -ray SED. A distinct trend in the boundaries on the spectral index diagrams in Figs. 1 and 3 are found for the PLLP model that can be tested with Fermi-LAT analyses in different energy ranges.

The Γ_γ vs. ν_s boundaries defined by the dominance of internal SSC or external EC IR or EC BLR processes have, furthermore, a very different shape when $b = 1$ (Fig. 2) compared to $b = 0.5$ (Fig. 1). This can be tested by subdividing the Fermi-LAT γ -ray spectral indices in different ranges of b . Whether the log-parabola function or the PLLP model, eq. (12) with a low-energy electron

index $s = 2$, better approximates the EEDs can be tested by searching for Fermi-LAT sources with $\Gamma_\gamma < 1.5$.

The weak dependences of Γ_γ on changes in L_{syn} found in eqs. (5) and (8) are consistent with the weak dependences of γ -ray spectral index Γ_γ on L_γ on either side of the blazar divide. A physical explanation for the change of the radiation environment of blazars at $\approx 0.01 L_{Edd}$, though a reasonable model assumption, would make sense of the blazar divide.

This leaves open the blazar sequence relations, which can ultimately only be understood from the physics occurring in the magnetospheres of the supermassive black holes powering the blazars. Near-equipartition blazar synchrotron sources with $\nu_s \gg 10^{15}$ Hz would suffer increasingly strong radiation pressure in an environment with dense external radiation fields, which could explain the absence of HSP FSRQs. Supermassive black-hole jets are most luminous when their emissions are coolest, that is, when their peak synchrotron and Compton frequencies are lowest. The near-equipartition log parabola blazar model provides a constrained system that explains the spectral-index diagrams, and points to studies that could allow for a deeper understanding of the blazar sequence and blazar divide.

The work of C.D.D. and J.D.F. is supported by the Chief of Naval Research. We thank Dr. Matteo Cerruti for discussions about spectral fitting, and the anonymous referee for constructive questions and the recommendation to consider the PLLP model.

APPENDIX

A. δ -FUNCTION THOMSON-REGIME SSC DERIVATION WITH LOG-PARABOLA EED

We derive the form of the νL_ν SED for the SSC component in the Thomson regime assuming a log-parabola function of the EED and employing δ -function approximations for synchrotron and Thomson scattering. The comoving Thomson-scattered synchrotron self-Compton spectrum for isotropic distributions of photons and nonthermal relativistic electrons is given by

$$\epsilon'_1 L'_{SSC}(\epsilon'_1; \Omega') = \frac{1}{2} m_e c^3 \epsilon'^2_1 \int_1^\infty d\gamma' \int_0^\infty d\epsilon' \int_{-1}^1 d\mu' (1 - \mu') N'_e(\gamma') n'_{ph}(\epsilon') \frac{d\sigma(\bar{\epsilon})}{d\epsilon'_1}. \quad (A1)$$

Here, μ' is the cosine of the angle between the directions of the interacting electron and photon, $\bar{\epsilon} = \gamma\epsilon'(1 - \mu')$ is the invariant collision energy, and $d\sigma(\bar{\epsilon})/d\epsilon'_1$ is the differential scattering cross section. We use the δ -function Thomson scattering cross section $d\sigma(\bar{\epsilon})/d\epsilon'_1 = \sigma_T \delta[\epsilon'_1 - \gamma'^2 \epsilon' (1 - \mu')]$ (eq. (6.44); Dermer & Menon 2009). From eq. (1), $N'_e(\gamma') = K' y^{-2-b \log y} / \gamma'^2_{pk}$, and the photon spectral density $n'_{ph}(\epsilon') = \epsilon' L'(\epsilon') / 4\pi f_0 R_b'^2 \epsilon'^2 m_e c^3$, where f_0 is a geometry factor, $R'_b = c \delta_D t_{var}$, and $t_{var}(1+z)$ is the measured variability time (Dermer et al. 2014a). For the synchrotron target photon spectrum, $\epsilon' L'_{syn}(\epsilon') = \epsilon L_{syn}(\epsilon) / \delta_D^4 = \nu x^{1-b \log x} / \delta_D^4$. Plugging these expressions into eq. (A1), and using the δ -function to solve the μ' integral, we find

$$\epsilon'_1 L'_{SSC}(\epsilon'_1; \Omega') = \frac{\sigma_T \nu K'}{\delta_D^4 4\pi f_0 R_b'^2 \gamma'^2_{pk} \epsilon'^3_{pk}} \int_{1/\gamma'_{pk}}^\infty dy y^{-6-b \log y} \int_{x_\ell}^\infty dx x^{-6-b \log x}. \quad (A2)$$

Here $x_\ell \equiv \sqrt{A}/y$, where $A = \epsilon'_1 / 2\gamma'^2_{pk} \epsilon'_{pk} = \epsilon / \epsilon_{pk,SSC}$. The interior integral can be solved by noting, to good approximation, the logarithmic term is slowly varying compared to the x^{-6} term. The value of this integral is then $x_\ell^{-5-b \log x_\ell} / 5$. After some manipulations, we obtain

$$\epsilon L_{SSC}(\epsilon; \Omega) \cong \frac{2\sigma_T \nu K' \gamma'_{pk}}{5\pi f_0 R_b'^2} \sqrt{\frac{\pi \ln 10}{2b}} A^{\frac{1}{2} - \frac{b}{8} \log A}. \quad (A3)$$

Comparing with eqs. (3) and (4) shows that the SSC spectral index is given by eq. (4) with b replaced by $b/2$ and ϵ_{pk} by $\epsilon_{pk,SSC}$, leading to eq. (8).

B. JET POWER IN THE NEAR-EQUIPARTITION LOG-PARABOLA MODEL

We consider jet power with the addition of baryons and photons. The baryon-loading factor $\eta_{bl} \equiv u'_{p/i}/u'_e$, and $\zeta_e \equiv u'_e/u'_{B'}$, where $u'_{p/i}$ is the fluid energy density of both thermal and nonthermal protons and ions, and u'_e is the nonthermal lepton energy density, including both electrons and positrons. For convenience, the thermal electron and positron energy density is assumed small. The absolute jet power for a two-sided jet is given by (Celotti & Fabian 1993; Celotti & Ghisellini 2008; Ghisellini & Tavecchio 2010)

$$L_{jet} = 2\pi r_b'^2 \beta \Gamma^2 c u'_{B'} [1 + \zeta_e(1 + \eta_{bl})] + L_{ph}, \quad (B1)$$

where the absolute photon power L_{ph} comprises synchrotron and SSC radiations, each assumed to be emitted isotropically in the jet frame, and EC radiations, with its comparatively narrower beaming (Dermer 1995). The absolute photon powers depend on the observing angle θ through the Doppler factor δ_D (Ghisellini & Tavecchio 2010; Dermer et al. 2012), giving the absolute jet power in the NELP model:

$$L_{jet}(\text{erg s}^{-1}) = (1 + N_\Gamma^2)^2 \{4.0 \times 10^{44} \sqrt{f_1 \sqrt{\frac{f_2 t_4}{\nu_{14}} \sqrt{\frac{L_{48}^5}{f_0 \zeta_s}}}} \left[\frac{1}{\sqrt{\zeta_e}} + \sqrt{\zeta_e(1 + \eta_{bl})} \right] + \frac{2(L_{SSC}^{iso} + L_{syn}^{iso})}{3\delta_D^2} + \frac{2L_{EC}^{iso}}{5\delta_D^2} (1 + N_\Gamma^2)^2 \} \quad (B2)$$

where the observing angle $\theta \equiv N_\Gamma/\Gamma \ll 1$ and $\Gamma \gg 1$. In this expression, L_{syn}^{iso} , L_{SSC}^{iso} , and L_{EC}^{iso} are the measured apparent isotropic bolometric synchrotron, SSC, and EC luminosities, respectively. The other two terms in eq. (B2) correspond to the magnetic-field, $\propto 1/\sqrt{\zeta_e}$, and the particle power, $\propto \sqrt{\zeta_e(1 + \eta_{bl})}$. The additional factor of $(1 + N_\Gamma^2)^2$ narrows the focus of the γ -ray beam. Eq. (B2) can be rewritten as

$$L_{jet}(\text{erg s}^{-1}) = 4.0 \times 10^{44} (1 + N_\Gamma^2)^2 \frac{L_{48}^{5/8} f_1^{1/2}}{(f_0 \zeta_s)^{1/8}} \left(\frac{f_2 t_4}{\nu_{14}} \right)^{1/4} \sqrt{(1 + \eta_{bl})(1 + \eta_{ph})} \left(\frac{1}{w} + w \right), \quad (B3)$$

where

$$w \equiv \sqrt{\frac{\zeta_e(1 + \eta_{bl})}{1 + \eta_{ph}}}, \quad (B4)$$

and the radiation loading

$$\eta_{ph} \equiv \frac{u'_{rad}}{u'_{B'}} = 5.4 f_0 \zeta_s [1 + \zeta_s + 0.6 \mathcal{A}_{EC} (1 + N_\Gamma^2)^2]. \quad (B5)$$

The isotropic bolometric photon luminosity $L_{ph}^{iso} = L_{syn}^{iso} + L_{EC}^{iso} + L_{SSC}^{iso} = \eta_{ph} L_{syn}^{iso}$, where the external Compton dominance $\mathcal{A}_{EC} = L_{EC}^{iso}/L_{syn}^{iso}$.

From eq. (B3), the minimum power condition is defined by the condition $w = 1$. When the baryon loading factor $\eta_{bl} \ll 1$ and the radiation loading $\eta_{ph} \ll 1$, the minimum power condition is defined by $\zeta_e = 1$. If the baryon-loading is arbitrary, but $\eta_{ph} \ll 1$, the minimum power condition is defined by $\zeta_e = 1/(1 + \eta_{bl})$. When $\eta_{bl} \gg 1$, the minimum power condition also corresponds to a highly magnetized jet (in terms of the electron energy density), with a larger jet luminosity by a factor $\sqrt{1 + \eta_{bl}}$ at minimum jet power compared to a pure electron/positron jet. When η_{bl} and η_{ph} take arbitrary values, the minimum power condition is defined by $\zeta_e = (1 + \eta_{ph})/(1 + \eta_{bl})$, and the minimum jet power increases $\propto \sqrt{(1 + \eta_{bl})(1 + \eta_{ph})}$.

Eq. (B3) gives the absolute minimum power to make the observed radiations from a blazar jet. For example, if the angular extent θ_j of the jet exceeds $1/\Gamma$, the power is increased by $\approx (\Gamma \theta_j)^2$. When observing at $\theta \approx 1/\Gamma$, the minimum jet power, $L_{jet} \approx 3 \times 10^{45} L_{48}^{5/8} \text{ erg s}^{-1}$ can only be increased by one to two orders of magnitude before exceeding $L_{Edd} \approx 1.3 \times 10^{47} M_9 \text{ erg s}^{-1}$ for a $10^9 M_\odot$ black hole, unless one demands unusually high photon efficiencies. For HSP BL Lac objects, with $L_{syn} \lesssim 10^{46} \text{ erg s}^{-1}$, there is no great difficulty in satisfying the Eddington limit, even far from equipartition. However, these very same objects are believed to be accreting at a rate $\lesssim 0.01 L_{Edd}$, so even in this case, large departures from equipartition cannot be tolerated.

Based on Fermi-LAT data, Ghisellini et al. (2014) argue that the absolute jet power P_{jet} is larger than the accretion-disk luminosity, which is approximated as 10 times the BLR luminosity. They also approximate $P_{jet} \approx 10 P_{rad}$, with the absolute radiation power $P_{rad} \approx k_f L_\gamma^{iso}/\Gamma^2$, where the factor $k_f = 8/3$ for synchrotron/SSC processes and $k_f = 32/5$ for EC processes, and the bulk Lorentz factor Γ of the radiating jet's plasma outflow is stated to be in the range $10 \lesssim \Gamma \lesssim 15$. The underlying assumption is that the observer is looking at $\theta_0 = 1/\Gamma$ to the jet axis. Inspection of the photon power in eq. (B3) shows how uncertain this assumption is given how much brighter fluxes are along the jet axis compared to fluxes from sources at $\theta_0 \approx 1/\Gamma$. Using the relation $1 + N_\Gamma^2 = 2\Gamma/\delta_D$, the photon power in eq. (B2) for a 2-sided jet is

$$P_{rad} = (1 + N_\Gamma^2)^4 \frac{L_{syn} + L_{SSC}}{6\Gamma^2} + (1 + N_\Gamma^2)^6 \frac{L_{EC}}{10\Gamma^2}. \quad (B6)$$

When viewing down the jet axis, these powers are ≈ 16 (synchrotron/SSC) and ≈ 64 (for EC) times less than the values used in the expression for P_{rad} by Ghisellini et al. (2014). The most powerful γ -ray sources have the largest core

dominances and brightness temperatures (e.g., Pushkarev et al. 2009; Kovalev et al. 2009; Li et al. 2014, however, see Savolainen et al. (2010)), suggesting that these sources are also the ones viewed almost along the jet axis. Indeed, Jorstad et al. (2005), Fig. 25, find no blazar with viewing angle $\theta_0 > 2/\Gamma$, whereas a large number of both BL Lacs and FSRQs have $\theta_0 < 1/2\Gamma$. A severe overestimation of the radiation and therefore jet power is made by not taking this effect into account.

For very powerful FSRQs like 3C 454.3, which has $L_{48} \sim 1$, a curious feature arises. Great flares exceeding $L_{EC}^{iso} \gtrsim 10^{50}$ erg s $^{-1}$ with large Compton dominance $\gtrsim 100$ can be allowed while maintaining absolute jet power $L_{jet} \lesssim L_{Edd}$ only if $\theta \ll 1/\Gamma$ and $\zeta_s \ll 1$, that is, $L_{syn}^{iso} \gg L_{SSC}^{iso}$, implying a small SSC component relative to the synchrotron component. The effect of decreasing ζ_s is to increase δ_D and narrow the Doppler cone, making the beaming factor even smaller, so that extreme apparent EC γ -ray powers lead to absolute jet powers that are sub-Eddington. Spectral modeling to give the relative SSC and EC powers depends on X-ray observations, for example, Swift and NuSTAR, Fermi-LAT observations at GeV energies, and ground-based VHE air Cherenkov arrays.

REFERENCES

- Abdo, A. A., Ackermann, M., Ajello, M., et al. 2009, *ApJ*, 700, 597
- Abdo, A. A., Ackermann, M., Ajello, M., et al. 2010a, *ApJ*, 715, 429
- Abdo, A. A., Ackermann, M., Agudo, I., et al. 2010b, *ApJ*, 716, 30
- Abdo, A. A., Ackermann, M., Ajello, M., et al. 2010c, *ApJS*, 188, 405
- Abdo, A. A., Ackermann, M., Ajello, M., et al. 2011, *ApJ*, 727, 129
- Ackermann, M., Ajello, M., Baldini, L., et al. 2010, *ApJ*, 721, 1383
- Ackermann, M., Ajello, M., Allafort, A., et al. 2011, *ApJ*, 743, 171
- Ackermann, M., Ajello, M., Atwood, W., et al. 2015, submitted to *ApJ*, arXiv:1501.06054
- Aharonian, F., Akhperjanian, A. G., Bazer-Bachi, A. R., et al. 2007, *ApJ*, 664, L71
- Ajello, M., Romani, R. W., Gasparrini, D., et al. 2014, *ApJ*, 780, 73
- Albert, J., Aliu, E., Anderhub, H., et al. 2007, *ApJ*, 669, 862
- Aleksić, J., Antonelli, L. A., Antoranz, P., et al. 2011, *ApJ*, 730, L8
- Becker, P. A., Le, T., & Dermer, C. D. 2006, *ApJ*, 647, 539
- Błażejowski, M., Sikora, M., Moderski, R., & Madejski, G. M. 2000, *ApJ*, 545, 107
- Bloom, S. D., & Marscher, A. P. 1996, *ApJ*, 461, 657
- Blumenthal, G. R., & Gould, R. J. 1970, *Reviews of Modern Physics*, 42, 237
- Böttcher, M., & Dermer, C. D. 2002, *ApJ*, 564, 86
- Böttcher, M., Dermer, C. D., & Finke, J. D. 2008, *ApJ*, 679, L9
- Böttcher, M., Harris, D. E., & Krawczynski, H., eds. 2012, *Relativistic Jets from Active Galactic Nuclei* (Berlin: Wiley)
- Cavaliere, A., & D’Elia, V. 2002, *ApJ*, 571, 226
- Celotti, A., & Fabian, A. C. 1993, *MNRAS*, 264, 228
- Celotti, A., & Ghisellini, G. 2008, *MNRAS*, 385, 283
- Cerruti, M., Dermer, C. D., Lott, B., Boisson, C., & Zech, A. 2013, *ApJ*, 771, LL4
- Chen, L. 2014, *ApJ*, 788, 179
- Dermer, C. D. 1995, *ApJ*, 446, L63
- Dermer, C. D., Murase, K., & Takami, H. 2012, *ApJ*, 755, 147
- Dermer, C. D., & Razzaque, S. 2010, *ApJ*, 724, 1366
- Dermer, C. D., Cerruti, M., Lott, B., Boisson, C., & Zech, A. 2014a, *ApJ*, 782, 82
- Dermer, C. D., Murase, K., & Inoue, Y. 2014b, *Journal of High Energy Astrophysics*, 3, 29
- Dermer, C. D., & Schlickeiser, R. 2002, *ApJ*, 575, 667
- Dermer, C. D., & Menon, G. 2009, *High Energy Radiation from Black Holes* (Princeton University Press)
- Dermer, C. D., Schlickeiser, R., & Mastichiadis, A. 1992, *A&A*, 256, L27
- Essey, W., Kalashev, O. E., Kusenkov, A., & Beacom, J. F. 2010, *Physical Review Letters*, 104, 141102
- Farrar, G. R., & Gruzinov, A. 2009, *ApJ*, 693, 329
- Finke, J. D. 2013, *ApJ*, 763, 134
- Fossati, G., Maraschi, L., Celotti, A., Comastri, A., & Ghisellini, G. 1998, *MNRAS*, 299, 433
- Fossati, G., Buckley, J. H., Bond, I. H., et al. 2008, *ApJ*, 677, 906
- Georganopoulos, M., Kirk, J. G., & Mastichiadis, A. 2001, *ApJ*, 561, 111
- Georganopoulos, M., & Kazanas, D. 2003, *ApJ*, 594, L27
- Ghisellini, G., Maraschi, L., & Tavecchio, F. 2009, *MNRAS*, 396, L105
- Ghisellini, G., Celotti, A., Fossati, G., Maraschi, L., & Comastri, A. 1998, *MNRAS*, 301, 451
- Ghisellini, G., & Tavecchio, F. 2009, *MNRAS*, 397, 985
- Ghisellini, G., & Tavecchio, F. 2010, *MNRAS*, 409, L79
- Ghisellini, G., Tavecchio, F., Maraschi, L., Celotti, A., & Sbarrato, T. 2014, *Nature*, 515, 376
- Ghisellini, G., Tavecchio, F., & Chiaberge, M. 2005, *A&A*, 432, 401
- Giommi, P., Padovani, P., & Polenta, G. 2013, *MNRAS*, 431, 1914
- Giommi, P., Padovani, P., Polenta, G., et al. 2012, *MNRAS*, 420, 2899
- Guilbert, P. W., Fabian, A. C., & Rees, M. J. 1983, *MNRAS*, 205, 593
- Hayashida, M., Madejski, G. M., Nalewajko, K., et al. 2012, *ApJ*, 754, 114
- Hillas, A. M. 1984, *ARA&A*, 22, 425
- de Jager, O. C., Harding, A. K., Michelson, P. F., et al. 1996, *ApJ*, 457, 253
- Jorstad, S. G., Marscher, A. P., Lister, M. L., et al. 2005, *AJ*, 130, 1418
- Kovalev, Y. Y., Aller, H. D., Aller, M. F., et al. 2009, *ApJ*, 696, L17
- Lewis, A., & Bridle, S. 2002, *PhRvD*, 66, 103511
- Li, S. H., Fan, J. H., & Wu, D. X. 2014, *Journal of Astrophysics and Astronomy*, 35, 467
- Liu, J., Yuan, Q., Bi, X. J., Li, H., & Zhang, X. M. 2012, *PhRvD*, 85, d3507
- Maraschi, L., Ghisellini, G., & Celotti, A. 1992, *ApJ*, 397, L5
- Marscher, A. P., & Gear, W. K. 1985, *ApJ*, 298, 114
- Massaro, E., Perri, M., Giommi, P., & Nesci, R. 2004, *A&A*, 413, 489
- Massaro, E., Perri, M., Giommi, P., Nesci, R., & Verrecchia, F. 2004a, *A&A*, 422, 103
- Massaro, E., Tramacere, A., Perri, M., Giommi, P., & Tosti, G. 2006, *A&A*, 448, 861
- Meyer, E. T., Fossati, G., Georganopoulos, M., & Lister, M. L. 2011, *ApJ*, 740, 98
- Meyer, E. T., Fossati, G., Georganopoulos, M., & Lister, M. L. 2012, *ApJ*, 752, LL4
- Paggi, A., Massaro, F., Vittorini, V., et al. 2009, *A&A*, 504, 821
- Peng, Y., Yan, D., & Zhang, L. 2014, *MNRAS*, 442, 2357
- Pushkarev, A. B., Kovalev, Y. Y., Lister, M. L., & Savolainen, T. 2009, *A&A*, 507, L33
- Sambruna, R. M., Maraschi, L., & Urry, C. M. 1996, *ApJ*, 463, 444
- Savolainen, T., Homan, D. C., Hovatta, T., et al. 2010, *A&A*, 512, AA24
- Shaw, M. S., Romani, R. W., Cotter, G., et al. 2013, *ApJ*, 764, 135
- Sikora, M., Begelman, M. C., & Rees, M. J. 1994, *ApJ*, 421, 153
- Sikora, M., Stawarz, L., Moderski, R., Nalewajko, K., & Madejski, G. M. 2009, *ApJ*, 704, 38
- Stawarz, L., & Petrosian, V. 2008, *ApJ*, 681, 1725
- Takami, H., Murase, K., & Dermer, C. D. 2013, *ApJ*, 771, LL32
- Tavecchio, F., & Ghisellini, G. 2008, *MNRAS*, 386, 945
- Tramacere, A., Massaro, F., & Cavaliere, A. 2007, *A&A*, 466, 521
- Tramacere, A., Giommi, P., Perri, M., Verrecchia, F., & Tosti, G. 2009, *A&A*, 501, 879
- Tramacere, A., Massaro, E., & Taylor, A. M. 2011, *ApJ*, 739, 66
- Waxman, E. 2004, *New Journal of Physics*, 6, 140
- Yan, D., Zeng, H., & Zhang, L. 2012, *MNRAS*, 424, 2173
- Yan, D., Zhang, L., Yuan, Q., Fan, Z., & Zeng, H. 2013, *ApJ*, 765, 122
- Yuan, Q., Liu, S., Fan, Z., Bi, X., & Fryer, C. 2011, *ApJ*, 735, 120
- Zhou, Y., Yan, D., Dai, B., & Zhang, L. 2014, *PASJ*, 66, 12